PAPER

Cobalt-doping in Cu_2SnS_3: enhanced thermoelectric performance by synergy of phase transition and band structure modification†

Huiwen Zhao,[a] Xiaoxuan Xu,[a] Chao Li,[b] Ruoming Tian,[c] Ruizhi Zhang, [iD][d] Rong Huang,[b] Yinong Lyu,[a] Dongxu Li,[a] Xiaohui Hu,[a] Lin Pan*[a] and Yifeng Wang [iD] *[a]

Mohite-type ternary sulfide Cu_2SnS_3, which has been intensively studied in the photovoltaic field, has recently attracted much attention as an outstanding p-type eco-friendly thermoelectric material. In the present work, significant synergistic effects of d-orbital-unfilled transition metal (Co) doping on the crystal structure and electrical/thermal properties of Cu_2SnS_3 are reported. Crystal structure evolution with Co doping, involving not only monoclinic to cubic and tetragonal transitions but also the formation of a hierarchical architecture (Cu–S nano-precipitates, metal and S vacancies, and even nano-scaled stacking faults), is related to bond softening and intensified phonon scattering. Thus, an ultralow lattice thermal conductivity of 0.90 W m^{-1} K^{-1} at 323 K to 0.33 W m^{-1} K^{-1} at 723 K was obtained. Moreover, an increased effective mass is derived from the contribution of the Co 3d states to the inherent Cu 3d and S 3p states in the valence band, leading to a remarkable power factor (0.94 mW m^{-1} K^{-2}, $x = 0.20$ at 723 K) with optimal doping. As a result, the high ZT of ~0.85 at 723 K elevates the modified Cu_2SnS_3 to the level of state-of-the-art mid-temperature eco-friendly sulfide thermoelectric materials.

Introduction

Thermoelectric (TE) materials can realize conversion between thermal gradient and electricity voltage; therefore, they have great potential in energy saving and environmental protection through waste heat harvesting.[1–3] The performance of TE materials, which essentially determines their conversion efficiency, is usually characterized by the dimensionless figure of merit $ZT = S^2\sigma T/(\kappa_e + \kappa_l)$, where S, σ, T, κ_e and κ_l are the Seebeck coefficient, electrical conductivity, absolute temperature, electronic thermal conductivity and lattice thermal conductivity, respectively.

Ideal TE materials should have high values of σ and S to achieve a large power factor (PF = $S^2\sigma$); at the same time, they should have an intrinsic low thermal conductivity to maximize

ZT. However, it is challenging to decouple these interrelated parameters. For this purpose, many approaches to enhance PF have emerged in the past decades. For example, band engineering to converge the valence (or conduction) bands achieved high valley degeneracy, which led to a large Seebeck coefficient while maintaining high electrical conductivity.[4–6] Band flattening of n-type PbTe enabled higher Seebeck coefficients in La-doped than in I-doped samples at a given carrier concentration.[7] It should be noted that in order to achieve a high PF, σ should be maintained at a reasonably high level, leaving κ_e with limited reduction space in TE materials according to the Wiedemann–Franz law. Therefore, suppressing the lattice contribution has also become a primary mission for TE research towards achieving high ZT, which actually appears to be the driving factor for many newly reported breakthroughs. For example, weak bonding and heavy elements in materials tend to generate a large anharmonicity, resulting in low κ_l (In_4Se_3,[8] SnSe[9] and $AgSbTe_2$ (ref. 10)). Additionally, solids with fine particle sizes (down to the nanoscale) have been found to exhibit low thermal conductivities due to the effect of grain size, as smaller grains usually cause intensified scattering of phonons at grain boundaries. Moreover, hierarchical structures, *e.g.* atomic scale alloying, nanoscale endotaxial precipitates and mesoscale grain boundaries, can have stronger phonon scattering effects over wide wavelength and frequency ranges of phonons; this leads to very low κ_l values in PbTe-based materials, further resulting in greatly improved TE performance.[11]

[a]Nanjing Tech University, College of Materials Science and Engineering, Nanjing 210009, China. E-mail: linpan@njtech.edu.cn; yifeng.wang@njtech.edu.cn

[b]East China Normal University, Key Laboratory of Polar Materials and Devices, Shanghai 200062, China. E-mail: 52141213003@stu.ecnu.edu.cn

[c]Toyota Physical and Chemical Research Institute, Nagakute 480-1192, Japan

[d]Department of Physics, Northwest University, Xi'an 710069, China. E-mail: zhangrz@nwu.edu.cn

† Electronic supplementary information (ESI) available: All the formulas used in this paper; computation of DOS for undoped and Co-doped samples; XRD Rietveld refinement results for $Cu_2Sn_{1-x}Co_xS_3$ (Fig. S1 and S2 and Table S1); the stacking fault in $Cu_2Sn_{1-x}Co_xS_3$ (Fig. S3) XPS analysis of $Cu_2Sn_{1-x}Co_xS_3$ (Fig. S4). The ratio of σ and n for $Cu_2Sn_{1-x}Co_xS_3$ (Fig. S5). See DOI: 10.1039/c7ta07140j

This journal is © The Royal Society of Chemistry 2017

J. Mater. Chem. A, 2017, 5, 23267–23275 | 23267

As an eco-friendly sulfide TE material, the mohite-type ternary compound copper tin sulfide, Cu_2SnS_3 (CTS), has attracted great attention recently due to its phonon–glass–electron–crystal characteristics. Basically, CTS adopts polymorphic structures, including a high temperature cubic structure (isomorphic with cubic sphalerite ZnS) and low temperature tetragonal, monoclinic and triclinic phases.[12,13] Due to its complex crystallographic networks and soft bonding between the metal and S atoms with diverse and even random coordination configurations, CTS has low lattice thermal conductivity. Moreover, electronically, CTS possesses a relatively narrow but suitable band gap of 0.7 to 1.3 eV, which provides space for electrical transport optimization. The upper valence bands of CTS are mainly composed of Cu 3d orbitals and S 3p orbitals, while Sn atoms have no obvious contribution; this leads to a 3-dimensional Cu–S conductive network in the CTS lattice, as demonstrated by Xi et al.[14] and Zhai et al.[13] Recently, a moderately high ZT (0.58 at 723 K) by Zn-doping was reported in a study[15] in which crystal structures were induced in a cation-disordered state, resulting in low κ_l (0.4 W m^{-1} K^{-1} at ~700 K) approaching the theoretical minimum at high temperatures, while the band structure of CTS was minimally affected. These findings indicate that further improvement of TE performance for CTS should be directed by electronic strategies, including band engineering.

As a potential approach, d-unfilled transition metal doping can introduce additional energy states of these atoms to the original valence bands, leading to a modified band structure and different transport properties. As reported by Tang and Xiao et al., cobalt (Co, [Ar] $4s^23d^7$) doping for Sn ([Kr] $5s^24d^{10}5p^2$) sites as magnetic ions can result in enhanced entropy contributed by the degeneracy of the electronic configuration in real space, leading to simultaneous enhancement of the Seebeck coefficient and electrical conductivity.[16,17] Therefore, Co-doping is expected to enhance the density of states (DOS) of CTS by the participation of Co-3d in the Cu-3d and S-3p dominating hybridized valence bands, which can further improve the power factor.[18] Meanwhile, Co-doping can also adjust carrier concentration without unduly damaging the hole transport networks, allowing for optimization of the electrical transport properties of CTS.

In the present work, a series of dense ceramics of Co-doped Cu_2SnS_3 samples ($Cu_2Sn_{1-x}Co_xS_3$) were prepared and investigated in an attempt to clarify the effects induced by the strategy described above. The results revealed an enhancement of the DOS effective mass m^* in Co-doped CTS originating from the band structure modification with a large PF; with a phase transition upon doping from the original monoclinic structure to cubic and tetragonal structures, the lattice thermal conductivity was suppressed significantly due to bond softening and enhanced phonon scattering, which should be attributed to the special microstructure features in the doped samples (lattice relaxation, cation-disorder, nanoprecipitates, etc.). Finally, by virtue of the synergistic effects of phase transition and band structure modification, a strikingly high maximum ZT_{max} ~ 0.85 was obtained at 723 K; this strongly suggests the significant role of d-unfilled TM doping for CTS and the promising prospective of CTS as a good mid-temperature TE material.

Experimental

Powder samples of the Co-doped compound $Cu_2Sn_{1-x}Co_xS_3$ with nominal x values of 0, 0.05, 0.10, 0.15, 0.20, and 0.25 were prepared by high temperature reactions. First, high purity elementary powders of Cu, Co, Sn, and S in a mole ratio of $2 : x : (1 - x) : 3$ were sealed in evacuated silica tubes and were heated from room temperature to 920 °C at a rate of 5 °C min^{-1}; the mixtures were soaked at this temperature for 8 h, then rapidly cooled to 700 °C and maintained for 48 h, followed by natural cooling to obtain $Cu_2Sn_{1-x}Co_xS_3$ ingots that were finally ground into powder by hand in an agate mortar. The powders were then compacted into dense pellets (over 95% theoretical density) by spark plasma sintering (SPS) in a graphite die at 500 °C for 5 min under vacuum (<10 Pa) and an axial pressure of 50 MPa.

The phase compositions and crystal structures of the pellet samples were checked by X-ray diffraction (XRD) analysis with an ARL X'TRA diffractometer (SmartLab3, RIGAKU, Japan) using Cu Kα radiation. Fracture cross-sections of the SPS samples were observed by field-emission scanning electron microscopy (FE-SEM, FEI Nova NanoSEM 450). High resolution transmission electron microscopy (HRTEM) observations and selected-area electron diffraction (SAED) analyses were performed on an electron microscope operating at 200 kV (JEM-2100, JEOL, Japan). The Seebeck coefficients and electrical conductivities were measured in the radial direction of a bar-shaped specimen with dimensions of 10 mm × 3 mm × 3 mm by a conventional steady state method and a four-probe method, respectively, in He atmosphere at 323 to 723 K with a commercial system (LSR-3, Linsins). X-ray photoelectron spectroscopy (XPS) was performed with a Physical Electronics system (ESCALAB 250Xi) using a standard Al Kα source. Thermal conductivity (κ) was calculated by $\kappa = DdC_p$ (D and C_p can be seen in Fig. S7, ESI†), where the thermal diffusivity (D) was measured in the axial direction of a disk-shaped sample of Φ 10 mm × 1 mm using a Netzsch laser flash diffusivity instrument (LFA457, Netzsch, Germany); C_p is the specific heat capacity measured by differential scanning calorimetry (DSC: 200 F3, TA instruments), and d is the mass density measured using the Archimedes method. Hall effect measurements for carrier concentration were conducted with a van der Pauw configuration under vacuum using a ResiTest8300 system (Toyo Tech. Co., Japan). Sound velocity was detected by the ultrasonic pulse-echo method (Model 5800 PR, Olympus).

First principles theoretical calculations to verify the contributions of the Co 3d states to the inherent valence band of CTS were carried out based on monoclinic CTS, both non-doped and Co-doped ($x = 0.25$), using the Quantum-ESPRESSO package[19] and the Garrity–Bennett–Rabe–Vanderbilt (GBRV) high-throughput pseudopotential library.[20] The Perdew–Burke–Ernzerhof (PBE) functional was used along with ultrasoft pseudopotentials for all the atoms. A plane wave basis with a kinetic energy cutoff of 600 eV was used to ensure convergence in all the

23268 | J. Mater. Chem. A, 2017, 5, 23267–23275

This journal is © The Royal Society of Chemistry 2017

calculations. A k-point sampling of $3 \times 5 \times 7$ was used for the Cu_2SnS_3 unit cell; for larger cells, the k-mesh was reduced accordingly. The atomic positions were relaxed until all the force components on each atom were less than 10^{-3} atomic units. For density of states calculations, a denser k-point sampling of $5 \times 7 \times 11$ was used for the Cu_2SnS_3 unit cell.

Results and discussion

Compositions and crystal structures

The powder X-ray diffraction patterns of the undoped and Co-doped Cu_2SnS_3 samples at room temperature are shown in Fig. 1. No impurity peaks were observed for the pristine or Co-doped samples. An obvious structure transformation with increasing Co-doping level in $Cu_2Sn_{1-x}Co_xS_3$ can be clearly seen. The diffraction patterns of $Cu_2Sn_{1-x}Co_xS_3$ ($x = 0$, 0.05) conform to the monoclinic structure (PDF# 27-0198), where Cu, Sn and Co atoms are distributed in their specified tetrahedral sites separately in an ordered manner. Meanwhile, $Cu_2Sn_{1-x}Co_xS_3$ ($x = 0.10$) adopted a cubic structure (PDF# 89-2877), and the XRD patterns of $Cu_2Sn_{1-x}Co_xS_3$ ($x = 0.20$) matched well with the standard tetragonal structure (PDF# 89-4714). These two structures feature highly random metal atom occupation: in the tetragonal structure, the 4d and 2b sites are occupied by the composite atoms M1 [43.6(2) at% Sn + 56.4(2) at% Cu] and M2 [46.3(3) at% Sn + 53.7(3) at% Cu], respectively, and the 2a tetrahedral sites are occupied by the remaining Cu atoms; meanwhile, in the cubic structure, the tetrahedral sites become equivalent and are fully occupied by composite M3 atoms (66.7% Cu + 33.3% Sn), corresponding to a complete disordering of metal atoms in this structure. This type of order-to-disorder atomic rearrangement can play a very significant role in phonon scattering, as has been found in many disordered systems.[21–23]

It is noteworthy that the XRD Rietveld refinement results (Fig. S1 and Table S1, ESI†) showed that the doped samples very likely have multiphase compositions; when x is increased from 0.05 to 0.25, the fraction of monoclinic phase decreases (from 46.15% to 2.57%) and the fractions of the tetragonal and cubic
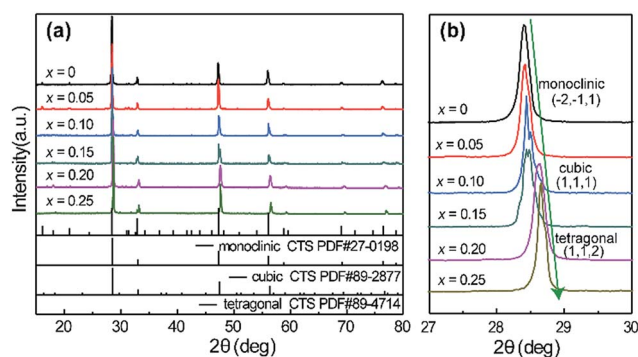
phases increase rapidly (from 53.85% to 97.43%). The lattice constants a and c and the M–S bond lengths obtained from refinement results are shown in Fig. S2 (ESI†). The results indicate that the lattice constant a decreases gradually with Co amount and that c is not greatly affected; meanwhile, the short M–S bond lengths in the pristine monoclinic phase are largely relaxed to a unified range in the cubic and tetragonal phases, which gives rise to bond weakening.

Strikingly, the (111) peak position for cubic phase (as well as the (112) peak position for tetragonal phase) shifted toward the higher angle side rather than toward the lower angle side, which is in contrast to the radius order of $r_{Co^{2+}}$ (58 pm at CN = 4) > $r_{Sn^{4+}}$ (55 pm at CN = 4). This suggests a much more complicated mechanism involving not only the simple replacement of Co for Sn in CTS, for which a process is proposed as follows starting from the octet rule: this rule states that if the sum of the valence electrons, Σ, of the cations surrounding an anion divided by the anion's coordination number plus the number of the anion's valence electrons is equal to eight, then that structure will be in a low energy state because the anion is in a closed-shell state. In the pristine monoclinic structure, S(1)-[3Cu,Sn] and S(2)-[3Cu,Sn] clusters, both with Σ values equal to 7, are connected by a S(3)-[2Cu,2Sn] cluster ($\Sigma = 10$) to minimize deviation from the octet rule, forming a tri–tetrahedra cluster with a total $\Sigma = 24$, i.e. an average of 8 for each of the 3 tetrahedra (there are 3 different S sites in the monoclinic structure, namely S(1), S(2) and S(3), as shown in Fig. 2(a) and (b); all of these are surrounded by 4 metal atoms, M, to form SM$_4$ clusters with different combinations of M). When Co^{2+} ions

Fig. 1 (a) Powder X-ray diffraction patterns of $Cu_2Sn_{1-x}Co_xS_3$ ($x = 0.05$ to 0.25) samples; (b) enlargements of the 27 to 30° regions with the ($-2-11$) peak of monoclinic phase, the (111) peak of cubic phase, and the (112) peak of tetragonal phase.
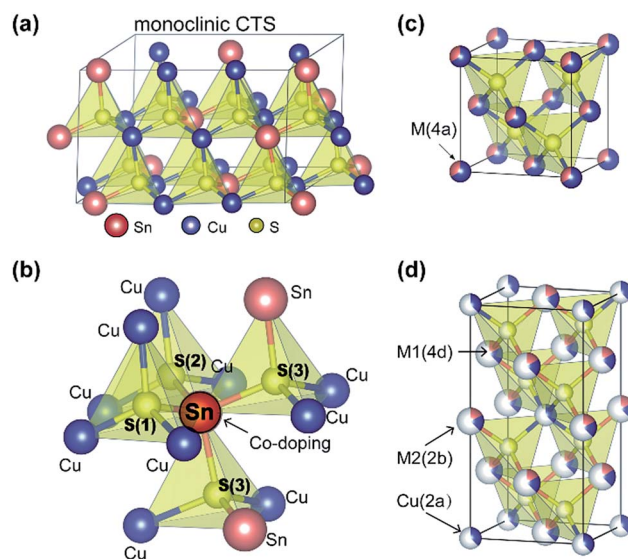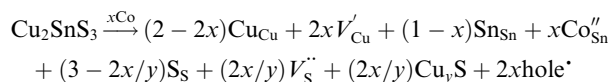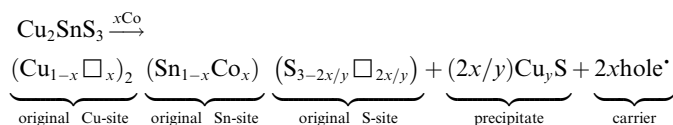

Fig. 2 Structural illustrations of (a) the monoclinic CTS structure, where metal atoms are fixed separately and in good order; (b) the location of Sn atoms inside monoclinic CTS, which bridge one S(1), one S(2) and two S(3) atoms, indicating that when a Sn atom is replaced by Co, the adjacent S(1)- and S(2)-centred tetrahedral would have a reduced $\Sigma = 5$ or 6; (c) the cubic CTS structure, where metal atoms are randomly distributed at the M (4a) sites; (d) the tetragonal CTS structure, where the 2a sites are occupied by Cu and the remaining 2b and 4d sites are occupied randomly by Cu, Sn and Co atoms.

substitute the Sn^{4+} ions as designed, S-[2Cu,Sn,Co] tetrahedra surrounded with two Cu atoms, one Sn atom and one Co atom are formed preferentially to reach $\Sigma = 8$ and lower the internal energy. However, this disrupts the local neutrality of the two adjacent tetrahedrals, S-[3Cu,Sn] originally, by forming S-[3Cu,Co] clusters ($\Sigma = 5$ or 6) with increased internal energies. In order to minimize the internal energy, 2 Cu atoms, one for each of the two S-[3Cu,Co] clusters, are "driven out" by 2 Sn atoms, forming 2 S-[2Cu,Sn,Co] clusters with $\Sigma = 8$, vacancies of Cu and S, and precipitates of Cu_yS. This whole process, as expressed below, would take place throughout the CTS crystal lattice toward the lowest-energy state, with the atomic ratio of Cu : Sn : Co approaching 2 : 1 : 1 as the Co substitution proceeds.

$$Cu_2SnS_3 \xrightarrow{xCo} (2-2x)Cu_{Cu} + 2xV'_{Cu} + (1-x)Sn_{Sn} + xCo''_{Sn}$$
$$+ (3 - 2x/y)S_S + (2x/y)V''_S + (2x/y)Cu_yS + 2x\text{hole}^\cdot$$

or

$$Cu_2SnS_3 \xrightarrow{xCo}$$
$$\underbrace{(Cu_{1-x}\square_x)_2}_{\text{original Cu-site}} \underbrace{(Sn_{1-x}Co_x)}_{\text{original Sn-site}} \underbrace{(S_{3-2x/y}\square_{2x/y})}_{\text{original S-site}} + \underbrace{(2x/y)Cu_yS}_{\text{precipitate}} + \underbrace{2x\text{hole}^\cdot}_{\text{carrier}}$$

In order to confirm the microstructure evolution of Cu_2SnS_3 with Co doping, the $Cu_2Sn_{1-x}Co_xS_3$ ceramic samples with $x = 0$, 0.05 and 0.20 were selected for SEM (Fig. S3, ESI†) and TEM observations. As can be seen from the fracture cross-section SEM images, the samples are highly dense and the grain sizes of samples are quite large, about several microns to tens of microns. Fig. 3(a) shows a typical HRTEM image and the corresponding FFT pattern of the pure CTS sample, which can only

be indexed to the [100] zone axis of monoclinic phase. Fig. 3(b) exhibits the HRTEM image and the corresponding FFT pattern of the 5% Co-doped CTS sample. This was indexed as the [110] zone axis of cubic phase. Meanwhile, stacking faults on the[22] planes were found in the 5% Co-doped CTS sample, as shown in Fig. 3(c) and S4, ESI.† The selected-area electron diffraction pattern with elongated diffraction spots (inset of Fig. 3(c)) clearly demonstrates the existence of stacking faults. Fig. 3(d) shows that some nanoprecipitates were distributed in the 20% Co-doped CTS sample. Significantly, these nanoscale domains can also introduce abundant additional phonon scattering sources and lead to low κ_1, as discussed in the following context.

As demonstrated above, the transition of the crystal structure would involve not only the substitution of Co at Sn-sites, but also the formation of Cu and S vacancies, Cu_yS precipitates and hole carriers. Therefore, due to the smaller size of Sn^{4+} (55 pm at CN = 4) than Cu^+ (60 pm at CN = 4) and to the vacancies formed, although Co^{2+} (58 pm at CN = 4) is slightly larger than Sn^{4+} (55 pm at CN = 4), the lattice would contract upon Co-doping, which agrees with the observed peak shifting of the XRD patterns. Thus, the nominal Co-doping at the Sn-site would first cause the rearrangement of Cu, Co, and Sn atoms and even Cu and S vacancies. Due to the similar crystallographic nature of the Cu atoms that are available for replacement by Sn, the rearrangement throughout the CTS tends to be highly disordered, which is actually the case in the obtained cubic and tetragonal CTS structures. Second, the Co-doping promoted the precipitation of Cu, which was actually found in all the doped CTS samples in the form of Cu_yS nano-precipitates, and even some stacking faults. Third, holes as the major carriers are created proportionally to the Co-doping amount x, which enables tunability of the electrical transport properties.

Electrical transport properties

The temperature dependences of electrical conductivity for all the samples are shown in Fig. 4(a). With increasing temperature from 323 K to 723 K, the electrical conductivity of the doped samples tends to decrease gradually, which suggests metallic behavior in contrast to undoped Cu_2SnS_3. Because of the existence of Co^{3+} (Fig. S5, ESI†) in $Cu_2Sn_{1-x}Co_xS_3$, the σ values of the Co-doped samples are smaller than those of the Zn-doped samples with the same x. Also, the gradual change of σ vs. T excludes the possible crystal structure transition at elevated temperatures, which occurs in many binary sulfides and selenides.[23,24] This is beneficial for long-term stable operation of TE devices.

Additionally, the σ values increase dramatically with increasing content of Co doping, even up to 1500 S cm^{-1} at 323 K with $x = 0.25$. As proven by Hall effect measurements, this is mainly due to an increase in carrier concentration (see Table 1), reflecting the essential role of Co acceptors in the doping process (although stacking faults, Cu and S vacancies and Cu_yS precipitates are also involved). The carrier mobility was found to decrease slightly as the Co amount increased, probably as a result of intensified electron scattering due to Cu_yS precipitates, other defects and carriers which form more commonly at
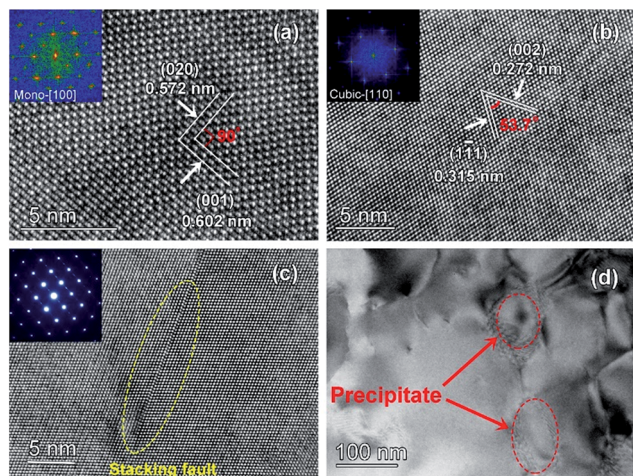

Fig. 3 Microstructure evolution of pure CTS to 20% Co-doped CTS: typical HRTEM images and the corresponding FFT patterns (insets) of (a) pure CTS with a monoclinic structure along the [100] zone axis; (b) 5% Co-doped CTS with a cubic structure along the [110] zone axis; (c) typical HRTEM image and the SAED pattern of the stacking faults in the 5% Co-doped CTS sample; and (d) low magnification TEM image of the nanoprecipitates in 20% Co-doped CTS.
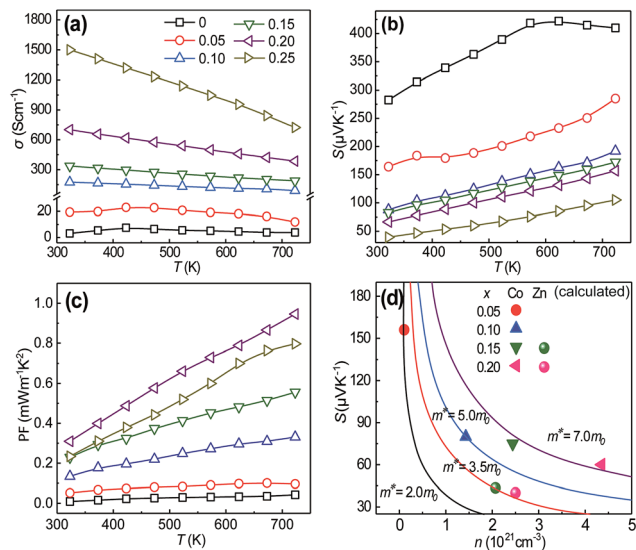
23270 | *J. Mater. Chem. A*, 2017, **5**, 23267–23275

This journal is © The Royal Society of Chemistry 2017

Fig. 4 Temperature dependence of (a) electrical conductivity, (b) Seebeck coefficient, (c) power factor of $Cu_2Sn_{1-x}Co_xS_3$ compounds (x = 0 to 0.25, 323 K to 723 K). (d) Pisarenko plot of Seebeck coefficient *versus* hole concentration in the Co-doped CTS samples at around 300 K, with simulated lines with effective mass $m^* = nm_0$ (n = 2.0, 3.5, 5.0 and 7.0). The increasing m^* with x suggests that the Co doping level makes a marked contribution to the density of electronic states of Cu_2SnS_3.

higher Co-doping levels, while the interfaces between the different CTS phases were not greatly affected, as observed previously. Moreover, the σ and n values (Fig. S6, ESI†) showed almost linear increases with x up to as high as 0.20, without the obvious drop that is often observed in heavily doped semiconductors; this may indicate the participation of Co-3d orbitals in these compounds. This would contribute to enhanced S values, as discussed below. Fig. 4(b) shows the Seebeck coefficient, S, as a function of temperature for the $Cu_2Sn_{1-x}Co_xS_3$ (x = 0 to 0.25) samples. All the Co-doped samples show positive S as p-type semiconductors. With increasing content of Co as an acceptor, the S values decrease gradually, from 282 $\mu V K^{-1}$ (x = 0) to 40 $\mu V K^{-1}$ (x = 0.25) at 323 K, suggesting a dominant effect of the growth of carrier concentration n rather than other factors, including m^*. In general, these values are modest when x is no less than 0.10; this reflects high n, which contributes to high σ, as shown in Fig. 4(a). In contrast to the anomalous temperature dependence in the undoped sample due to thermal excitation of bipolarons,[15] the S values in the doped samples all undergo a continuous and steadily increase as the temperature increases, as expected for materials with substantial band gaps.

Table 1 Carrier concentration n and mobility μ from Hall effect measurements at 300 K for the doped samples

Sample	x = 0.05	x = 0.10	x = 0.15	x = 0.20
n (10^{21} cm^{-3})	0.11	1.43	2.44	4.35
μ (cm^2 V^{-1} S^{-1})	1.13	1.59	1.46	1.01

As a result, high power factors can still be obtained due to the high σ values at high temperatures.

Fig. 4(c) shows PF as a function of temperature for the $Cu_2Sn_{1-x}Co_xS_3$ (x = 0 to 0.25) samples. The PF of the Co-doped samples increases with increasing doping content from x = 0.05 to x = 0.20. However, the PF of $Cu_2Sn_{0.75}Co_{0.25}S_3$ decreased slightly because of the rapid decrease of the Seebeck coefficient. The maximum PF (0.94 mW m^{-1} K^{-2} at 723 K) is obtained when x = 0.20, which appears to be surprisingly large compared with most sulfide TE materials.[25–27]

To clarify the origin of the high PF, the experimental data for S and n of Co-doped CTS in comparison with Zn-doped analogues were used to calculate the DOS effective mass m^* based on the single parabolic band (SPB) model, which should be maintained at a high n over 10^{21} cm^{-3} for these heavily doped CTS samples.[14] As shown in Fig. 4(d), the obtained m^* value increases from 2.0 at x = 0.05 to (5.0–7.0) m_0 for x = (0.1 to 0.2), and is strikingly larger than that of Zn-doped compounds (around $3.5m_0$) at high x. In part, this may be related to the enhanced doping level, which corresponds to a deeper Fermi level inside the valence band corresponding to a larger DOS in CTS, as has previously been experimentally and theoretically interpreted.[15] More importantly, it is very likely that the Co-3d sub-orbitals participate in the valence bands to give rise to a further increase of m^*. Relevant calculations regarding the larger m^* leading to enhanced DOS in Cu_2CoSnS_4 have been reported.[18] In Cu_2CoSnS_4, a small portion of the energy states due to the hybridization between the Co 3d-states and S 3p-states appeared near the valence band edge, in addition to the main contribution from the hybridized Cu-3d and S-3p orbitals, which serve as a conducting pathway for holes. Additionally, in a spinel sulfide of $CuCo_2S_4$, the Co-3d orbitals in the valence band are even located above the Cu-3d states, which indicates that the Co 3d states may have been hybridized with those of Cu-3d and S-3p. For the case of CTS doping, in contrast to Zn^{2+} ([Ar] $3d^{10}$), which has a filled 3d electronic shell, Co^{2+} cations ([Ar] $3d^7$) have 3 unpaired 3d sub-orbitals available for hole transport; thus, the substitution of Co for Sn^{4+} ([Kr] $4d^{10}$) would lead to hybridization of the 3d orbitals of Co with the S 3p orbitals in the unoccupied bands (d–p antibonding bands). Therefore, additional pathways for holes between the S atoms originally bridged with Sn atoms are built (it should be noted that the connection of S–Sn–S is not beneficial for hole conduction because there is no obvious contribution from Sn at the conduction band), leading to an additional increase of DOS and further growth of m^*. Therefore, the enhancement of m^*, which is even higher than that for Zn-doping, originates from the increase of n as a result of acceptor doping, and more importantly from the contribution of the Co-3d orbitals to the valence bands at the Fermi level.

DOS calculations based on first principles theories greatly support the above assumption. The DOS enhancement contributed by the Co 3d orbital is shown in Fig. 5 using blue lines. The DOS near the valence band maximum was enhanced by the contribution from both the up and down-spinning states of the Co-3d orbitals, which is expected to be responsible for the higher PF. As CTS is not magnetic, the up and down DOS are the
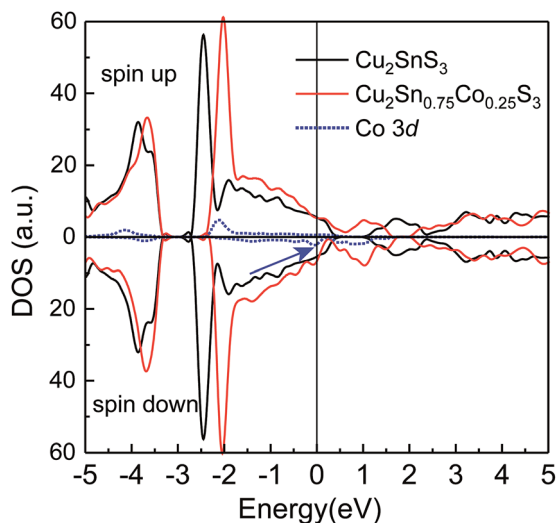
This journal is © The Royal Society of Chemistry 2017

J. Mater. Chem. A, 2017, **5**, 23267–23275 | **23271**

Fig. 5 The density of states of undoped and Co-doped Cu_2SnS_3 ($x = 0.25$), where a noticeable contribution of down-spin Co-3d states can be seen.

same; however, after Co doping, the up and down DOS are different. The DOS of the two systems are aligned based on the inner sulfur 3s orbital, and the dashed line is the Fermi energy only for a doped system. It can be seen that near the Fermi energy, the DOS of the doped system is slightly larger than that of the non-doped system, which is beneficial for a larger Seebeck coefficient. Incidentally, it should be worthwhile to further investigate the influence of doping on the band gap; this will be carried out in subsequent research.

Thermal conduction properties

Fig. 6(a) shows the total thermal conductivity (κ) as a function of temperature for the $Cu_2Sn_{1-x}Co_xS_3$ ($x = 0$ to 0.25) samples. The κ value for all the samples decreases gradually with increasing temperature, which is indicative of dominant phonon–phonon interactions with increasing temperature. The κ for pristine

CTS, ranging from 2.4 W m^{-1} K^{-1} at room temperature to 0.8 W m^{-1} K^{-1} at 723 K, is highly comparable with those reported in the literature. For the doped samples, the κ values increased with x in the whole temperature range, which is indicative of considerable contributions from the electrical conduction. Except for the Co-doped ($x = 0.25$) sample, the values for the doped samples are smaller than that of the undoped sample, suggesting that much stronger phonon scattering occurred inside them. Moreover, these values are quite low at high temperatures and are even comparable with the best TEs.

To obtain better insight into the origin of the variation of κ, the electronic thermal conductivity (κ_e) is estimated from the Wiedeman–Franz law as $\kappa_e = L\sigma T$, where the Lorenz number L was obtained from the reduced chemical potential η, which was calculated from the experimental S and n data (see the calculation details and Fig. S8, ESI†). As shown in Fig. 6(a), the κ_e values are quite constant in the whole temperature range, while they increase remarkably with x. For the undoped sample, κ_e is negligible to the total κ, indicating the primary role of phonon conduction in this value. Meanwhile, for the doped CTS, the values increased form 0.02 W m^{-1} K^{-1} ($x = 0.05$) to 1.1 W m^{-1} K^{-1} ($x = 0.25$) at 323 K due to the higher σ and L values in the more heavily doped samples.

By subtracting κ_e from κ, the lattice thermal conductivity (κ_l) was calculated; this is shown in Fig. 6(b) as a function of temperature. As can be seen, the κ_l values for all the doped samples ($x = 0.05$ to 0.25) are very close to each other and are very small. These values decrease gradually, following a T^{-1} dependence indicative of Umklapp type phonon–phonon interaction as the predominating phonon scattering mechanism, from $\sim$0.9 W m^{-1} K^{-1} at 323 K to 0.3–0.4 W m^{-1} K^{-1} at 723 K, a level close to the theoretical minimum of 0.3 W m^{-1} K^{-1}. This is not a rare phenomenon, as ultralow κ_l values have been reported in many papers for similar diamond-like ternary sulfide TEs.[28,29] Because the grain size is quite large for all the samples, grain boundary phonon scattering should be ruled out as the primary mechanism. However, the mechanism appears to be very complicated, in consideration of the fact that there
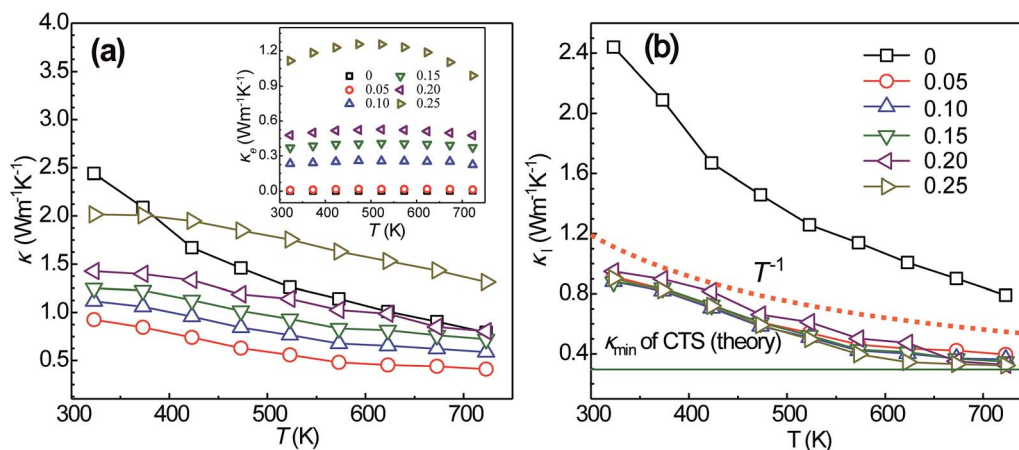

Fig. 6 Temperature dependence of (a) thermal conductivity; (b) lattice thermal conductivity of the $Cu_2Sn_{1-x}Co_xS_3$ ($x = 0$ to 0.25) bulk materials. The insert figure displays the electronic thermal conductivities of the $Cu_2Sn_{1-x}Co_xS_3$ ($x = 0$–0.25) bulk materials.

23272 | *J. Mater. Chem. A*, 2017, **5**, 23267–23275

This journal is © The Royal Society of Chemistry 2017

are various phonon scattering behaviors in these compounds, including soft bonds, mass-disorder, random atomic arrangements, vacancies, phase interfaces, grain boundaries and stacking faults. Here, we propose an explanation based on the phonon velocity and phonon mean free path.

Based on the kinetic theory of gases, κ_l can be expressed as $\kappa_l = 1/3 C_v v_{avg} l_p$, where C_v is the volumetric specific heat, v_{avg} is the average speed of sound and l is the phonon mean free path. Furthermore, the density (ρ), Grüneisen parameter (γ), Young's modulus (E), shear modulus (G), bulk modulus (B) and phonon mean free path (l) of each sample were calculated and are listed in Table 2.

It is clearly demonstrated that upon Co-doping, the v_t, v_l and v_{avg} sound velocities are reduced by ~18% compared to that of the pristine sample, although the density is only reduced by about 2%; moreover, the moduli E, G and B are reduced by about 30% to 48%. These results tend to reveal a weakening of interatomic forces and increased anharmonicity in the Co-doped compounds. However, the calculated Grüneisen parameters are all about 1.7 to 1.9; these values are high but comparable to each other. Therefore, interatomic force softening is the primary mechanism of the reduction of the sound velocities and elastic modulus, and it likely occurs for three reasons. First, there should be a weaker electrostatic force of attraction between Co^{2+} and S^{2-} than between Sn^{4+} and S^{2-} because the bond lengths of metal atoms to S atoms become unified after doping; for example, the short Cu–S bonds in pristine CTS, which are around 2.17 to 2.28 Å (less than the sum of the ionic radii of M and S due to overlapping by attraction forces), are relaxed to become comparable with the long bonds of 2.35 Å (nearly equal to the sum of the ionic radii of M and S) in the cubic and tetragonal CTS after doping (Fig. S2(b), ESI†). Second, the formation of Cu and S vacancies would result in additional weakening of the atomic interactions; third, the Cu_yS precipitates can also slow the passage of phonons due to their superionic nature, according to Shi et al.[30] Thus, the bonds in the materials as a whole are softened upon Co-doping, leading to a decrease in the speed of sound. It is also interesting to see that the sound velocities and even the elastic modulus are very close to the data for Cu_yS,[30] which has an ultralow lattice thermal conductivity of about 0.3 W m^{-1} K^{-1}.

On the other hand, the l values are very small as a result of the high anharmonicity in CTS, either pristine or doped. This value was observed to drop from 1.36 to ~0.5 nm with increasing doping amount of x from 0 to 0.20. First, the random

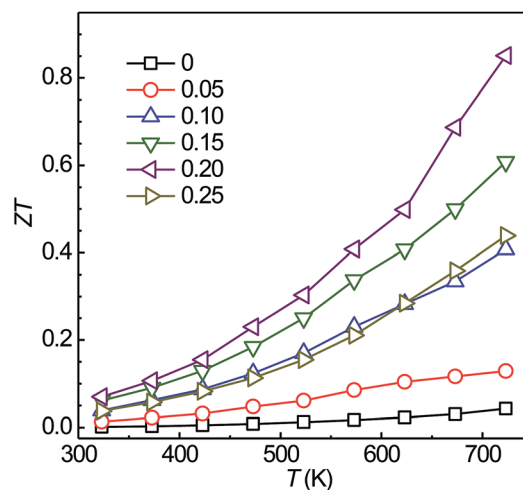**Fig. 7** Temperature dependence ZT of the $Cu_2Sn_{1-x}Co_xS_3$ ($x = 0$ to 0.25) bulk materials from 323 K to 723 K.

occupation of the metal atoms (atom number $Z = 27, 50, 29$ for Cu, Sn, and Co, respectively) and even the M and S vacancies in the cubic structure (completely disordered) and tetragonal structure (partially disordered) may thoroughly disrupt the normal phonon transport,[15] leading to a glass-like random walk of phonons within a spatial distance close to the distance of the neighboring M atoms (the average distance between two M atoms is about 0.4 nm); second, the vacancies caused by Co doping and the phase boundaries of different CTS structures and even the interfaces between the defect region and the main body of the matrix will further interrupt the phonon transport. Furthermore, the presence of Cu_yS nano-precipitates will also disturb the normal propagation of phonons.

Thus, Co-doping in CTS leads not only to weakening of the interatomic attraction forces, which suppresses the elastic modulus and sound velocities, but also to enhanced hierarchical phonon scattering, which lowers the phonon mean free path, enabling substantially reduced κ_{lat} (0.85 W m^{-1} K^{-1} at 323 K, and ~0.33 W m^{-1} K^{-1} at 723 K, which is close to its theoretical minimum value of ~0.3 W m^{-1} K^{-1}).

Dimensionless figure of merit

From the above parameters, the dimensionless figure of merit values, ZT, of $Cu_2Sn_{1-x}Co_xS_3$ ($x = 0$ to 0.25) were calculated and are shown in Fig. 7. It was found that the ZT values increase with

Table 2 Parameters of density ρ, transverse v_t, longitudinal v_l, average speed of sound v_{avg}, Young's modulus E, shear modulus G, bulk modulus B, Grüneisen parameter γ, and phonon mean free path l of the bulk $Cu_2Sn_{1-x}Co_xS_3$ materials ($x = 0$ to 0.20) at 300 K

x	ρ (g cm^{-3})	v_l (m s^{-1})	v_t (m s^{-1})	v_{avg} (m s^{-1})	γ	E (GPa)	G (GPa)	B (GPa)	l (nm)
0	4.58	4648	2373	2658	1.93	64.53	24.37	61.01	1.36
0.05	4.52	3687	1968	2198	1.78	38.07	14.63	31.85	0.76
0.10	4.46	3940	2015	2257	1.92	45.12	17.05	42.46	0.70
0.15	4.43	3540	1924	2146	1.71	33.61	13.02	26.73	0.63
0.20	4.53	3872	1988	2227	1.91	44.01	16.66	40.98	0.44

This journal is © The Royal Society of Chemistry 2017

J. Mater. Chem. A, 2017, **5**, 23267–23275 | **23273**

increasing temperature in the measured temperature range. Moreover, the ZT values of the Co-doped samples are much higher than that of pristine CTS within the whole temperature range. An unexpectedly high ZT value (~ 0.85) was observed for the $Cu_2Sn_{0.8}Co_{0.2}S_3$ sample at 723 K; this is a fairly high value among Cu-based ternary sulfide TE materials, such as $CuFe_{0.9}Sb_{0.1}S_2$ ($ZT_{623\ K} \sim 0.19$),[25] $Cu_4Sn_7S_{16}$ ($ZT_{700\ K} \sim 0.2$),[26] $CuFeS_{1.8}$ ($ZT_{573\ K} \sim 0.21$),[31] and Cu_5FeS_4 ($ZT_{900\ K} \sim 1.2$).[28]

Conclusion

Mohite-type ternary sulfide Cu_2SnS_3 was investigated for TE performance by doping with d-orbital-unfilled Co at the Sn site, with emphases on the synergistic effects of crystal and band structure variations. The structural variation due to Co-doping is very complicated, involving not only the evolution of pristine monoclinic symmetry to doped cubic and tetragonal structures, but also the formation of Cu–S precipitates, stacking faults and even M and S vacancies. A weakening of M–S interatomic bonding induced by the phase transition was deduced from sound velocity analysis; this results in a strong reduction of the phonon velocities and elastic modulus. Primarily, due to complex structures in the doped samples, phonon scattering is greatly intensified, giving rise to a small mean free path close to the distance of two neighboring M atoms (0.4 nm). The lattice thermal conductivity is very low, 0.90 W m^{-1} K^{-1} at 323 K and ~ 0.33 W m^{-1} K^{-1} at 723 K. These findings regarding the microstructure and the lattice thermal conductivity are expected to aid material structure design in the TE research community.

Electrically, 3d-unfilled Co substitution for Sn enhances both n and m^* due to the acceptor role of Co and, likely, the participation of Co-3d near the Fermi level in the upper valence band, which leads to enhancement of S accompanied with a high σ with doping. PF reaches a maximum value of 0.94 mW m^{-1} K^{-2} at 723 K for $x = 0.20$. Due to the increase of PF and the decrease of κ_{lat}, an unexpectedly high ZT of 0.85 at 723 K was achieved for $Cu_2Sn_{0.8}Co_{0.2}S_3$; this is much higher than the values achieved for other sulfide materials[18,25,32] that have been reported to date. Thus, Co-doped CTS is a very competitive eco-friendly candidate for mid-temperature TE applications.

Author contributions

H. Zhao, X. Xu and Y. Wang designed the experiments; H. Zhao, X. Xu, R. Huang, C. Li, Y. Lv, P. Lin, D. Li, and Y. Wang performed the material syntheses and sample measurements; R. Tian did the Hall effect measurement and analysis; R. Zhang and X. Hu contributed to the calculations. All authors discussed the results and commented on the manuscript. Everyone was involved in writing the paper.

Conflicts of interest

There are no conflicts to declare.

Acknowledgements

References

1 S. B. Riffat and X. Ma, *Appl. Therm. Eng.*, 2003, **23**, 913–935.

2 L. E. Bell, *Science*, 2008, **321**, 1457–1461.

3 W. Liu, Q. Jie, H. S. Kim and Z. Ren, *Acta Mater.*, 2015, **87**, 357–376.

4 Y. Pei, X. Shi, A. LaLonde, H. Wang, L. Chen and G. J. Snyder, *Nature*, 2011, **473**, 66–69.

5 Q. Zhang, H. Wang, W. Liu, H. Wang, B. Yu, Q. Zhang, Z. Tian, G. Ni, S. Lee, K. Esfarjani, G. Chen and Z. Ren, *Energy Environ. Sci.*, 2012, **5**, 5246–5251.

6 Y. Tang, Z. M. Gibbs, L. A. Agapito, G. Li, H. S. Kim, M. B. Nardelli, S. Curtarolo and G. J. Snyder, *Nat. Mater.*, 2015, **14**, 1223–1228.

7 Y. Takagiwa, Y. Pei, G. Pomrehn and G. J. Snyder, *Appl. Phys. Lett.*, 2012, **101**, 092102.

8 J. S. Rhyee, K. H. Lee, S. M. Lee, E. Cho, S. I. Kim, E. Lee, Y. S. Kwon, J. H. Shim and G. Kotliar, *Nature*, 2009, **459**, 965–968.

9 L. D. Zhao, S. H. Lo, Y. Zhang, H. Sun, G. Tan, C. Uher, C. Wolverton, V. P. Dravid and M. G. Kanatzidis, *Nature*, 2014, **508**, 373–377.

10 B. Du, H. Li, J. Xu, X. Tang and C. Uher, *Chem. Mater.*, 2010, **22**, 5521–5527.

11 K. Biswas, J. He, I. D. Blum, C. I. Wu, T. P. Hogan, D. N. Seidman, V. P. Dravid and M. G. Kanatzidis, *Nature*, 2012, **489**, 414–418.

12 M. Onoda, X. A. Chen, A. Sato and H. Wada, *Mater. Res. Bull.*, 2000, **35**, 1563–1570.

13 Y.-T. Zhai, S. Chen, J.-H. Yang, H.-J. Xiang, X.-G. Gong, A. Walsh, J. Kang and S.-H. Wei, *Phys. Rev. B: Condens. Matter Mater. Phys.*, 2011, **84**, 1303–1324.

14 L. Xi, Y. B. Zhang, X. Y. Shi, J. Yang, X. Shi, L. D. Chen, W. Zhang, J. Yang and D. J. Singh, *Phys. Rev. B: Condens. Matter Mater. Phys.*, 2012, **86**, 1722.

15 Y. Shen, C. Li, R. Huang, R. Tian, Y. Ye, L. Pan, K. Koumoto, R. Zhang, C. Wan and Y. Wang, *Sci. Rep.*, 2016, **6**, 32501.

16 G. Tang, T. Yang, X. Xu, C. Tang, L. Qiu, Z. Zhang, L. Lv, Z. Wang and Y. Du, *Appl. Phys. Lett.*, 2010, **97**, 032108.

17 C. Xiao, K. Li, J. Zhang, W. Tong, Y. Liu, Z. Li, P. Huang, B. Pan, H. Su and Y. Xie, *Mater. Horiz.*, 2014, **1**, 81–86.

18 D. Zhang, J. Yang, Q. Jiang, Z. Zhou, X. Li, J. Xin, A. Basit, Y. Ren and X. He, *Nano Energy*, 2017, **36**, 156–165.

19 P. Giannozzi, S. Baroni, N. Bonini, M. Calandra, R. Car, C. Cavazzoni, D. Ceresoli, G. L. Chiarotti, M. Cococcioni and I. Dabo, *J. Phys.: Condens. Matter*, 2009, **21**, 395502.

23274 | *J. Mater. Chem. A*, 2017, **5**, 23267–23275

This journal is © The Royal Society of Chemistry 2017

20 K. F. Garrity, J. W. Bennett, K. M. Rabe and D. Vanderbilt, *Comput. Mater. Sci.*, 2014, **81**, 446–452.

21 J. Fan, W. Schnelle, I. Antonyshyn, I. Veremchuk, W. Carrillo-Cabrera, X. Shi, Y. Grin and L. Chen, *Dalton Trans.*, 2014, **43**, 16788–16794.

22 J.-Y. Hwang, M.-W. Oh, K. H. Lee and S. W. Kim, *J. Mater. Chem. C*, 2015, **3**, 11271–11285.

23 Z.-H. Ge, L.-D. Zhao, D. Wu, X. Liu, B.-P. Zhang, J.-F. Li and J. He, *Mater. Today*, 2016, **19**, 227–239.

24 G. Dennler, R. Chmielowski, S. Jacob, F. Capet, P. Roussel, S. Zastrow, K. Nielsch, I. Opahle and G. K. H. Madsen, *Adv. Energy Mater.*, 2014, **4**, 1301581.

25 B. Du, R. Zhang, K. Chen, A. Mahajan and M. J. Reece, *J. Mater. Chem. A*, 2017, **5**, 3249–3259.

26 C. Bourgès, P. Lemoine, O. I. Lebedev, R. Daou, V. Hardy, B. Malaman and E. Guilmeau, *Acta Mater.*, 2015, **97**, 180–190.

27 P. Zawadzki, L. L. Baranowski, H. Peng, E. S. Toberer, D. S. Ginley, W. Tumas, A. Zakutayev and S. Lany, *Appl. Phys. Lett.*, 2013, **103**, 253902.

28 P. Qiu, T. Zhang, Y. Qiu, X. Shi and L. Chen, *Energy Environ. Sci.*, 2014, **7**, 4000–4006.

29 P. Qiu, X. Shi and L. Chen, *Energy Storage Mater.*, 2016, **3**, 85–97.

30 Y. He, T. Day, T. Zhang, H. Liu, X. Shi, L. Chen and G. J. Snyder, *Adv. Mater.*, 2014, **26**, 3974–3978.

31 J. Li, Q. Tan and J.-F. Li, *J. Alloys Compd.*, 2013, **551**, 143–149.

32 P. Mangelis, P. Vaqueiro, J.-C. Jumas, I. da Silva, R. I. Smith and A. V. Powell, *J. Solid State Chem.*, 2017, **251**, 204–210.

This journal is © The Royal Society of Chemistry 2017

J. Mater. Chem. A, 2017, **5**, 23267–23275 | **23275**